AIAA 2002-0845

Three-Dimensional Effects on Multi-Element High Lift Computations

Christopher L. Rumsey,
Elizabeth M. Lee-Rausch,
and Ralph D. Watson
NASA Langley Research Center
Hampton, Virginia

40th AIAA Aerospace Sciences Meeting & Exhibit
14-17 January 2002/Reno, NV

THREE-DIMENSIONAL EFFECTS ON MULTI-ELEMENT HIGH LIFT COMPUTATIONS

Christopher L. Rumsey,* Elizabeth M. Lee-Rausch,† and Ralph D. Watson‡
NASA Langley Research Center
Hampton, Virginia

Abstract

In an effort to discover the causes for disagreement between previous 2-D computations and nominally 2-D experiment for flow over the 3-element McDonnell Douglas 30P-30N airfoil configuration at high lift, a combined experimental/CFD investigation is described. The experiment explores several different side-wall boundary layer control venting patterns, documents venting mass flow rates, and looks at corner surface flow patterns. The experimental angle of attack at maximum lift is found to be sensitive to the side wall venting pattern: a particular pattern increases the angle of attack at maximum lift by at least 2°. A significant amount of spanwise pressure variation is present at angles of attack near maximum lift. A CFD study using 3-D structured-grid computations, which includes the modeling of side-wall venting, is employed to investigate 3-D effects on the flow. Side-wall suction strength is found to affect the angle at which maximum lift is predicted. Maximum lift in the CFD is shown to be limited by the growth of an off-body corner flow vortex and consequent increase in spanwise pressure variation and decrease in circulation. The 3-D computations with and without wall venting predict similar trends to experiment at low angles of attack, but either stall too early or else overpredict lift levels near maximum lift by as much as 5%. Unstructured-grid computations demonstrate that mounting brackets lower the lift levels near maximum lift conditions.

---

*Senior Research Scientist, Computational Modeling and Simulation Branch, Associate Fellow AIAA.

†Research Engineer, Computational Modeling and Simulation Branch.

‡Senior Research Scientist, Flow Physics and Control Branch, Senior member AIAA.

1 Introduction

A large number of CFD studies have been conducted for multi-element airfoil configurations over the last decade. Some of these pertained to experiments conducted in the NASA Langley low turbulence pressure tunnel (LTPT) for McDonnell Douglas 3-element configurations such as the 30P-30N. See, for example, refs. 1–5. The LTPT tests were nominally 2-D, obtained with the use of a side-wall boundary layer control system that applied suction near the model via venting through porous plates.[6] The CFD studies employed 2-D calculations when comparing with LTPT data.

Although CFD could claim some success in the prediction of the experimental multi-element flow field, certain key predictions were in error.[7] Most notably, CFD consistently predicted both the maximum lift and the angle of attack at which it occurs to be higher than experiment (e.g., at $\alpha = 23°$ as opposed to $\alpha = 21°$). Although turbulence models were originally suspected as a potential cause for this discrepancy, additional CFD studies with more advanced models[2,4,8] indicated that the differences between turbulence models tended to be relatively small for these cases.

A recent CFD control surface effectiveness study by Jiang[9] demonstrated that even nominally 2-D wind tunnel experiments with side-wall venting can have significant 3-D effects that are too large to ignore in CFD modeling. In an effort to determine if 3-D effects are the root cause of the disagreement between CFD and experiments for the 30P-30N near maximum lift, an investigation using a two-pronged approach was undertaken. The first effort was an experimental investigation that focused on the effects of side-wall venting and venting pattern on results near maximum lift, and included attempts to deduce flow features near the side walls using surface oil. Also, the experiment measured venting parameters, such as mass flow rate, that were not measured in earlier experiments on this configuration. The second effort involved modeling the 3-D configuration with CFD, including side-wall venting.

Sensitivity to venting suction levels was investigated and the flow field features near the side wall were examined. Additionally, CFD using unstructured grids was used to explore the effects of the mounting brackets on the 3-D flow field. This paper summarizes the results from this two-pronged study.

2 Description of the Experiment

The 30P-30N is a McDonnell Douglas Aerospace (MDA) 3-element configuration (designated LB546 in MDA's nomenclature). The model consists of the LS12 slat, the W10BB wing box assembly (main), and the F22 flap. The slat is at an angle of attack of $-30°$, with a gap of 2.95% c and overhang of -2.5% c. The flap is at an angle of attack of $30°$, with a gap of 1.27% c and overhang of 0.25% c. The configuration has a stowed chord length c of 22 in., and the LTPT tunnel width is 36 in. For all results to be shown below, the wing coordinates have been nondimensionalized by c. In this coordinate system, in the deployed position the leading edges of each element are located in the following positions: slat at $x/c = -0.0854$, main at $x/c = 0.0438$, flap at $x/c = 0.8715$. The 30P-30N configuration has been tested in the past at several different Reynolds numbers ranging from 5 million to 16 million, although the current experimental study only used Re = 9 million. The nominal Mach number in the current investigation is $M = 0.2$.

In an attempt to achieve the most 2-D flow field possible, porous plates were located at the side-walls of the LTPT near the wing.[10] The porous plates were connected to a venting chamber that vented out to the atmosphere through a remotely-operated ball valve. The default experimental procedure was as follows: during any set of given runs, the ball valve was adjusted (with the wing at an angle of attack of 16°) to minimize the spanwise pressure variation, as determined from several rows of spanwise pressure taps on the model. Then, at other angles of attack during the same series of runs, the valve remained open the same amount. In the current experiment, the effect of varying the venting mass flow rate at each angle of attack near maximum lift was also investigated. A no-venting configuration (all porous plates covered with tape) as well as 4 different porous plate configurations were tested; these are summarized in Table 1.

Sketches of the porous regions used in the experiment are depicted in Fig. 1. The porous region over the main element was not varied. It was approximately 0.5 inch high and began about 5 in. back from the element's leading edge on its upper surface and extended downstream until it connected in

Table 1. Summary of venting configurations in the current experiment

Config.	main venting	flap venting	strip in front of slat
1	no	no	no
2	yes	yes, widening	no
3	yes	yes, widening	yes
4	yes	yes, constant	no
5	yes	yes, constant	yes

a continuous fashion with the porous region over the flap. Two configurations over the flap were tested. The first ("widening") had the region over the flap widening from 0.5 inch to approximately 1.5 inch near the trailing edge. The second ("constant") employed the default pattern used in past tests (unpublished, but documented in LTPT engineer test notes), which kept the width over the flap constant at 0.5 inch. When employed, the porous region in front of the slat was a large semi-circular strip of width 1 inch, whose downstream inner radius touched the slat leading edge. The porous plate had 0.0625 inch diameter holes spaced 0.191 inch apart, for a porosity level of approximately 3–4%. In the experiment at Re = 9 million, the LTPT operating total pressure was approximately 54 psi. For most of the runs, unless otherwise noted, the Δp between the vent chamber and the tunnel (freestream) was approximately 8 psi.

3 Numerical Method

The compressible CFD codes used in the current investigation were CFL3D,[11] a structured-grid upwind finite-volume method, and FUN3D,[12,13] an unstructured-grid upwind finite-volume method. The turbulence model employed by both codes was the Spalart-Allmaras (SA) model, version Ia.[14] In CFL3D, transition was set on each of the elements at the following fixed locations for all runs: $x/c = -0.0261$ and -0.0847 on the slat lower and upper surface, $x/c = 0.6999$ and 0.0682 on the main lower and upper surface, and $x/c = 1.1243$ and 0.9214 on the flap lower and upper surface. These locations are representative of locations measured by Bertelrud,[15] but were not varied with angle of attack for this study. In CFL3D, transition was achieved by zeroing out the turbulence production term in the region of each grid zone where laminar flow is desired. All FUN3D runs assumed fully-turbulent flow.

In simulating wall venting (used for the CFL3D runs only), a linear form of the Darcy pressure-

velocity law was used:[16]

$$v_w = \frac{\sigma}{\rho_\infty u_\infty}(p_c - p_w),\qquad(1)$$

where p_c is the vent chamber pressure and σ is an "effective" geometric porosity factor. Thus, the wall venting suction velocity was assumed to be directly proportional to the difference between the vent chamber pressure (taken in this case to be constant) and the local pressure at the wall. However, there is still some uncertainty in the application of this law to the current case of the wing in the LTPT. The factor σ in Darcy's law is somewhat ad-hoc. It is proportional to the actual porosity level but is considerably larger in magnitude,[16] and is usually determined by comparison with measured wall velocities. In this study a range of values for σ from 0 – 0.3 in steps of 0.1 were used to determine their effect. Resulting mass flow through the vent was compared with experimentally measured levels to ascertain the approximate correspondence between the CFD and the experiment.

In the CFD runs, the nondimensional vent chamber pressure was assumed to be $p/(\rho_\infty a_\infty^2) = 0.62$, giving a ratio of the freestream static pressure to vent chamber static pressure of 1.152. The 30P-30N configuration and the locations on the side-wall where the Darcy law was applied are shown in Fig. 2. These venting regions approximate the regions employed in Config. 2 of the experiment.

For simplicity, the side wall venting pattern in the CFD study followed grid lines, which is the reason for the non-smooth boundary outline near the front of the flap in Fig. 2. The porous semi-circular region in front of the slat was not modeled in the CFD. A symmetry (slip) wall boundary condition was employed on the side-wall at and upstream of approximately $0.8c$ in front of the wing; thus, the side-wall boundary layer was relatively "fresh" at the start of the wing in the computations.

The top and bottom walls of the LTPT wind tunnel were not modeled in the current study. A previous study[17] explored the effects of including these walls in 2-D computations. The chief effect was to raise the upper surface pressures on the flap and on the aft end of the main at high angles of attack (yielding lower lift, not quantified in the reference). There was also an effect on the computed wake positions. The current structured grid extended approximately $15c$ above, below, in front of, and behind the wing, and far field Riemann boundary conditions were applied there. Also, symmetry was assumed in the wind tunnel, and only half of the span was modeled by the grid: one side modeled the tunnel wall, and the other side used symmetry boundary conditions to model the tunnel center plane.

The grid used by CFL3D was the same one employed in earlier 2-D CFD studies,[4,5] except that it was duplicated with 33 planes in the spanwise direction, with viscous clustering near the side-wall. There were 4 zones (with 1-to-1 point matching at interfaces) in the grid, with 135,425 nodes per plane, or 4.47 million total nodes. The minimum spacing near solid walls was between $0.2 - 3.1 \times 10^{-6}c$. The viscous unstructured grids had a far field extent of $10c$ and 846,863 nodes (no brackets), and 1.35 million nodes (including brackets). The minimum spacing near solid walls was $1 \times 10^{-6}c$.

4 Results

4.1 Experiment

The lift curves for the five configurations in the current tunnel entry are shown in Fig. 3. These values of lift were obtained by integrating the pressures from the taps located along the center of the model. As expected, Config. 1 (no wall venting) yields lower levels of lift at all angles of attack. However, somewhat surprisingly, the angle of attack at maximum lift is the same as most of the wall-venting runs ($\alpha = 21°$). It was originally thought that corner flow separation would cause an earlier stall in this case. Config. 2 also exhibited unexpected results: its maximum lift occurs at a *higher* angle of attack, $\alpha \geq 23°$, than all the other runs. Previously, the angle of attack for maximum lift had almost always come out to be $\alpha = 21°$. This result suggests that side-wall venting treatment can influence the physical process or mechanism(s) responsible for limiting maximum lift in the wind tunnel.

Fig. 4 shows the effect of different venting levels on the lift curve near maximum lift for Config. 2. Two separate entries are represented on this plot. The initial entry, which used $\Delta p = 8$ psi, is the same curve shown in Fig. 3. In a later entry, the Δp was varied at each angle of attack. Results using $\Delta p = 8$ psi are inconsistent with the initial entry, indicative of a hysteresis effect: in the initial entry, the lift continues to increase through $\alpha = 23°$, whereas in the other the maximum lift occurs at $\alpha = 22°$. In both the $\Delta p = 6$ psi and $\Delta p = 12$ psi cases, the lift continues to increase through $\alpha = 23°$.

From the last two figures, it is already clear that the flow field near maximum lift is very sensitive, and the angle of attack where maximum lift occurs can vary by 2° or more, depending on the side wall treatment (although the change in C_L is less than 1%). The "widening" venting pattern on the flap seems to be necessary to achieve higher angle of attack for

American Institute of Aeronautics and Astronautics

$C_{L,max}$. It is not known why including the slat strip (Config. 3) loses this advantage. One question that can be asked is whether the variation in maximum lift is a function of the three-dimensionality of the flow. Unfortunately, in the experiment we only have surface pressures to address this issue. Surface oil flow, discussed in greater detail below, showed no evidence of separated wing-wall juncture flow when wall venting was present. Off-surface flow visualization was not possible in this test.

Fig. 5 shows spanwise pressures on the flap upper surface at an unstowed chordwise location of $x/c = 0.925$, as a function of angle of attack for Configs. 2 and 4. The plot shows that as the angle of attack increases beyond $\alpha = 16°$, the flow field becomes less and less two-dimensional. It also appears that at the highest angles of attack, Config. 4 exhibits somewhat more three-dimensionality than Config. 2. In particular, the pressure variation is less "flat" near the tunnel center plane. This increased three-dimensionality is consistent with the fact that Config. 4 is unable to achieve as high a $C_{L,max}$ as Config. 2.

The pressures and the mass flow rate in the venting chambers were measured in this test. Ten pressures were taken at various locations behind each wall's plate to check for variations with position. Although not shown, these were found to vary by less than 0.2 psi at any given angle of attack. Also, the pressure levels varied by only a small amount, less than 0.8 psi, as the angle of attack was varied (generally the venting pressure increased at higher angles of attack). The mass flow rates as a function of angle of attack and configuration are shown in Fig. 6. When no leading edge slat venting is present, the mass flow rate is roughly 0.7 lb_m/sec. Including slat venting increases the mass flow rate to approximately 1.6 lb_m/sec.

When side-wall venting is employed, surface oil flow shows no indication of 3-D corner flow structures near maximum lift conditions. However, with solid side walls (no venting), significant deviation from 2-D flow at the walls near the corners could be seen at all angles of attack near maximum lift. An enhanced photograph is shown in Fig. 7 at $\alpha = 20°$. There is turning of the flow over both the main element and the flap away from the side wall, and there are several complex flow patterns indicating 3-D flow features on the side wall as well. At higher angles of attack, similar patterns exist, except the sizes and locations of the features vary somewhat. Oil was not applied at lower angles of attack.

4.2 Computations

4.2.1 Structured Grid Results

A compilation of the computed results are shown in Fig. 8 for Config. 1 (no venting) and Fig. 9 for Config. 2 (venting). In each figure, the experimental results are shown as solid symbols. 2-D results using CFL3D are shown for reference as a solid line, and 3-D results from the current study using CFL3D are shown as open symbols connected by lines. All lift levels from the 3-D computations are obtained by integrating the pressures in the tunnel center plane. When massive side-wall effects occur in the CFD (past the computed $C_{L,max}$), the flow generally goes unsteady. However, because steady-state time marching is employed, only representative lift coefficient values are shown to indicate that the angle of attack for maximum lift has been exceeded in the computations.

As shown in Fig. 8, when there is no venting modeled in the CFD, lift levels are lower than the 2-D levels. This is because 3-D flow features in the wall-juncture region lower the wing circulation. Results agree well with experiment up to roughly $\alpha = 16°$, but above this the CFD predicts massive side-wall effects and the lift drops dramatically. Clearly CFD is *not* showing the same character as the experiment at higher angles of attack. Surface streamlines at $\alpha = 19°$ are shown in Fig. 10. Compare with Fig. 7 (at a slightly higher angle of attack). Although results show similar character on the main element, flow over the flap and side wall is different. CFD indicates only small deviations from streamwise flow on the flap, whereas experiment shows a large separated region. However, the *surface* streamlines in this flow field are deceptive. The *off-body* streamlines for this case are shown in Figs. 11. There is a significant region of 3-D flow occurring *off the surface* above and behind the flap, the general shape of which shows a similar footprint to the photograph. In cases such as this one, for which a large off-body vortex is present, the current grid is probably too coarse to adequately resolve the flow feature. Fig. 12 shows vorticity contours along with a view of the spanwise grid in a vertical plane above the trailing edge of the flap. Grid underresolution likely contributes to over-spreading of the vortex and early stall in the computations.

When venting is modeled in the CFD, results agree with experiment at lower angles of attack, but are overpredicted compared to the experiment at higher angles of attack (see Fig. 9). Computed $C_{L,max}$ changes depending on the magnitude of the suction. Using $\sigma = 0.1$, $C_{L,max}$ occurs at $\alpha = 19°$, $\sigma = 0.2$ gives $C_{L,max} = 21°$, and $\sigma = 0.3$ gives

Table 2. Summary of CFD venting characteristics for Configs. 1 and 2

σ	mass flow, lb_{m}/sec	predicted $C_{L,max}, deg$
0.0	n/a	≈ 16
0.1	0.53	19
0.2	1.03	21
0.3	1.38	22

$C_{L,max} = 22°$. The higher the suction level, the closer the 3-D computation mimics 2-D computational results at the highest angles of attack. These results are summarized in Table 2, along with the corresponding mass flow rate computed to be exiting through the porous wall as a result of the Darcy pressure-velocity law boundary condition. Comparing these numbers with the mass flow rate from the experiment for Config. 2 (of approximately 0.7 lb_{m}/sec), it appears that a σ between 0.1 and 0.2 in the CFD would best represent the actual test. All computed results with venting for the rest of the paper use $\sigma = 0.2$.

Now let us examine results for several different angles of attack. Fig. 13 shows spanwise pressure coefficients on the flap at $\alpha = 4°$, both without and with side-wall venting. In the case of no venting, CFD accurately predicts the experimental level near the tunnel center plane, but the spanwise variation is overpredicted. CFD results on a coarser grid are also shown in the figure (grid using every other point in each coordinate direction); they exhibit little difference from results on the finer grid. When venting is simulated, CFD results again agree with the experimental results near the tunnel center plane; in this case the spanwise variation is small for both CFD and experiment.

Fig. 14 shows chordwise pressure coefficients at $\alpha = 4°$ for Config. 1 (no venting). CFD results are given at four span locations, and are compared with experimental results at the tunnel center plane (50% span). 2-D computed results are also shown for reference. CFD agrees well with the experiment at 50% span. The changes with span station exemplify the significant effects of the 3-D flow on the surface pressures near the back of the main element and on the flap. Fig. 15 shows chordwise pressure coefficients at $\alpha = 4°$ for venting Config. 2. Agreement at 50% span between CFD and experiment is again excellent, and results in this case also agree with 2-D computations. There is no noticeable spanwise variation in the computed results.

Figs. 16, 17, and 18 show spanwise and chord-wise pressure coefficients at $\alpha = 16°$, without and with venting. In this case, CFD results are *not* grid-independent between the medium and fine grids (Fig. 16). Also, the actual c_p levels for CFD and experiment at $x/c = 0.925$ on the flap do not agree; CFD yields somewhat lower levels in general. Similar to results at $\alpha = 4°$, the CFD results again show spanwise variation over the flap and back of the main for the no-venting case (Fig. 17), and very little spanwise variation for the venting case (Fig. 18). Other than small differences in the suction peaks and over the upper surface of the flap and back of the main, agreement with experimental c_p levels is fairly good overall.

Figs. 19, 20, and 21 show spanwise and chordwise pressure coefficients at $\alpha = 19°$, without and with venting. Again, the actual c_p levels for CFD and experiment at $x/c = 0.925$ on the flap do not agree; CFD yields lower levels in general. In Fig. 20, CFD for the no-venting case exhibits significant spanwise variation. This case has already stalled, and surface pressures do not agree at all with experiment, which does not reach $C_{L,max}$ until a higher angle of attack. CFD results with venting in Fig. 21 show no noticeable spanwise variation. Agreement with experiment is generally good, although CFD yields slightly stronger suction peaks than experiment and most of the flap upper surface and the back of the main is at slightly lower pressure. Results at higher angles of attack, with venting, show agreement/disagreement with experiment similar to Fig. 21. Plots of all three elements are not shown, but details can be seen in close-up views near the trailing edge of the main in Figs. 22 and 23. Here, the underprediction of pressure levels in this region is clearly seen.

The reason for CFD's increasing deviations from experimental trends near maximum lift is still unknown. Even with wall venting modeled, the lift either tends to be too high (as for $\alpha \geq 19°$ using $\sigma = 0.2$), or massive separation occurs and $C_{L,max}$ is reached too early (as occurs for lower levels of suction, e.g., $\sigma = 0.1$ in Fig. 9). Some of the deviations in upper surface pressure on the flap and back of the main may be due to the fact that the top and bottom walls were not modeled.[17] Nonetheless, the use of CFD appears to require a delicate balancing act of parameters to achieve a reasonable representation of the true 3-D physics.

In spite of these difficulties and uncertainties, it can be useful to use the CFD results (with venting) to explore the influence of the three-dimensional character of the flow field on $C_{L,max}$. In Fig. 22 at $C_{L,max} = 21°$, little spanwise variation is seen, but in Fig. 23 at $\alpha = 22°$ (past the predicted $C_{L,max}$),

5

spanwise variation is clearly starting to show up. Figs. 24, 25, and 26 show off-body streamlines for flow fields computed at three angles of attack with wall venting. At the two lower angles of attack up to and including $C_{L,max} = 21°$, there is off-body three-dimensional corner flow, but it is relatively small and its effect is localized. At $\alpha = 22°$, however, the three-dimensionality increases. Fig. 27 shows how significantly the character of the spanwise pressure changes at $\alpha = 22°$. (It also shows that the c_p values on the flap for the 2-D and 3-D computations, although indistinguishable at the scale shown in Fig. 18, really are slightly different at and above $\alpha = 16°$ at $x/c = 0.925$.)

In looking at Fig. 27, one might be tempted to declare that the flow at $\alpha = 22°$ is "2-D enough" on the portion of the wing near the center plane of the tunnel (because the curve is relatively flat at that location), but this view ignores the effect of the corner flow on the overall circulation of the wing system. When a significant region of corner flow circulation exists, there is a lower overall circulation around the wing, and the lift level decreases. In other words, $C_{L,max}$ in this case is limited by 3-D effects, and not by the 2-D mechanism conjectured in Ying et al.[5]

Comparing Fig. 27 with Fig. 5 from the experiment, it is seen that the two are *not* behaving similarly. Whereas the CFD spanwise variation remains relatively flat through $\alpha = 21°$, the experiment shows more evidence of 3-D flow even as low as $\alpha = 19°$. This difference probably explains why the experiment gives lower levels of lift as it approaches $C_{L,max}$. Unfortunately, we were not successful in simulating the conditions necessary to achieve this same degree of three-dimensionality in the CFD.

It should be noted that many of the 3-D CFD runs were dependent on the initial conditions. For example, if a high angle of attack run was restarted from a solution for which the flow was massively separated, results tended to *remain* highly separated. On the other hand, if restarted from a mostly-attached-flow solution, a high angle of attack run had a greater likelihood of remaining attached. This issue of non-uniqueness in the CFD solution for these flows is troubling. However, all runs for this study were conducted in "steady state" mode (i.e., non-time-accurate time marching was employed). It is possible that when significant regions of corner flow separation are present, then time-accurate approaches must be pursued in order to better represent the physics.

4.2.2 <u>Unstructured Grid Results</u>

The unstructured grid methodology was primarily employed for the purpose of investigating the effects of the mounting brackets on the solution near $C_{L,max}$. It was easier to make an unstructured 3-D grid to include brackets using VGRID[18] as opposed to creating a structured grid. However, even the unstructured grid generation process had limitations. It proved to be too difficult to create a sufficiently-refined viscous grid — with fine normal spacing near the wing, brackets, and in the wake regions — in the time allotted. In the end, the viscous grids used were somewhat too coarse to adequately represent the lift levels of this configuration (lift levels were about 8–12% lower than results on the fine structured grid). Therefore, this part of the CFD study should be regarded qualitatively only.

A view of the wing including mounting brackets is shown in Fig. 28. The unstructured grid on the side wall is also shown. There were a total of 8 brackets in the tunnel, four for the slat and four for the flap. The near-wall brackets (0.77 in. wide) were at 10.7% span, and the near-center brackets (0.09 in. wide) were at 36.8% span. This figure shows half of the model. Unstructured-grid results were obtained using both inviscid (Euler) equations (on grids with inviscid-type spacing near the wing) and viscous (Navier-Stokes) equations on the grid shown in the figure. The side wall was computed using inviscid boundary conditions in both cases. Resulting lift coefficients, from integration of the pressures along the center plane, are given in Fig. 29. The effects of the brackets on the inviscid solution are minimal, but the brackets lower the lift levels in the viscous computations by approximately 2–3%. Most of the effect is felt by the main element. This result is interesting in light of the fact that the structured CFD results (no brackets) tend to overpredict the lift levels near $C_{L,max}$ in the experiment. However, firm conclusions are not possible without additional study.

Computed streamlines for the $\alpha = 20°$ case with brackets, shown in Fig. 30, indicate some deviation from 2-D flow even relatively far away from the bracket span locations. Pressure coefficients as a function of span location are shown in Fig. 31 near the back of the main element. A noticeable spanwise variation is seen on the upper surface of the main and flap. Although not shown, when no brackets are present, there is very little variation.

5 <u>Summary and Conclusions</u>

In an effort to determine if 3-D effects were the root cause of previous disagreement between CFD

American Institute of Aeronautics and Astronautics

and experiments for the 30P-30N near maximum lift, a combination experimental/CFD investigation was undertaken. Unfortunately, even the 3-D CFD showed discrepancies from the experiment, especially at high angles of attack. In particular, CFD tended to either predict lift levels too high, or else stalled too early. This discrepancy may have been due to inadequate grid resolution (e.g., no attempt was made to grid-resolve the off-body corner-flow vortex), part to inadequate physical representation (e.g., not modeling the top and bottom walls, not representing the side-wall boundary layer inflow correctly, not including mounting brackets, not representing tunnel disturbances and asymmetries), and part to inadequacies in modeling (e.g., turbulence modeling, Darcy's pressure-velocity law boundary condition).

However, details aside, this study answered (or began to answer) some questions. The angle of attack of maximum lift in the experiment was clearly sensitive to side-wall venting shape. This fact strongly suggests that some flow feature near the side walls may be responsible for limiting $C_{L,max}$, rather than a purely 2-D mechanism. The 3-D CFD results indicated that this feature was probably an off-body corner-flow vortex that was present at high angles of attack even when side-wall venting was applied. It is consistent that the "widening" venting pattern in the experiment achieved the highest $C_{L,max}$, because the larger venting area over the flap would have had more of an influence on an off-body vortex.

A summary of major points from the experimental study were:

- A new venting pattern with a "widening" region of suction over the flap increased the angle of attack at maximum lift from $\alpha = 21°$ to at least $23°$.

- The application of different levels of suction (between 6 and 12 psi difference from the freestream tunnel total pressure) had relatively small effects (less than 1%) on lift levels near maximum lift.

- Above $\alpha = 16°$, there was a significant amount of spanwise pressure variation on the flap, even with side-wall venting present.

- When no side-wall venting was employed, lift coefficient levels dropped nearly uniformly by 0.1–0.2, but the angle of attack at maximum lift remained at $\alpha = 21°$.

- The mass flow rates through the side wall venting were quantified for the purposes of this and future 3-D CFD efforts.

A summary of major points from the CFD study were:

- The fine grid was probably sufficiently fine for use at the lower angles of attack, but its adequacy at higher angles of attack was dubious, particularly because of underresolution of the wall vortex.

- CFD with no side-wall venting could predict the character of the experiment at lower angles of attack. However, above $\alpha = 16°$, the CFD predicted massive 3-D corner flow features and consequently a loss of lift not seen in the experiment. The 3-D flow features were mostly off-body; *surface* streamlines over the flap were different in character from oil flow in the experiment.

- CFD with side-wall venting could predict the character of the experiment at lower angles of attack up through $\alpha = 16°$, but CFD (using enough suction to avoid early stall) tended to retain more spanwise two-dimensionality than experiment at higher angles of attack. Tunnel center plane pressures still agreed fairly well with experiment, but integrated lift near $C_{L,max}$ was generally overpredicted by as much as 5%.

- CFD yielded different angles of attack for $C_{L,max}$ depending on the side-wall suction level applied. The higher the suction, the closer the results of the 3-D simulation mimicked 2-D lift levels.

- The maximum lift achievable by CFD appeared to be directly related to the degree of three-dimensionality in the flow field. At and below $C_{L,max}$, the off-body corner flow features were relatively small and there was very little spanwise variation of surface pressures. Beyond $C_{L,max}$, the off-body corner flow features were larger and spanwise variation of surface pressures increased. This behavior was different in character from experiment, which exhibited large spanwise variation of surface pressures *prior* to $C_{L,max}$ as well as after.

- Darcy's law boundary condition required a σ parameter between 0.1 and 0.2 to achieve a similar mass flow rate as in the experiment.

American Institute of Aeronautics and Astronautics

- An investigation using unstructured grids indicated that the lift was reduced by approximately 2–3% near $C_{L,max}$ when brackets were included in viscous computations.

Aside from the points listed above, some general conclusions from this work were: (a) 2-D CFD should not be expected to agree with the nominally 2-D wind tunnel experiment at high lift conditions because the experiment lost its 2-D character at high angles of attack; and (b) 3-D CFD using the current grids and methodology compared well with experiment at low angles of attack, but did not adequately model the character of the wind tunnel flow field near maximum lift. To improve this deficiency, based on our experience we recommend that future 3-D CFD efforts for this configuration include (in order of importance):

- finer grid resolution in the region of the wall vortex, and overall finer resolution for unstructured grids

- top and bottom walls and mounting brackets

- better characterization of the incoming sidewall boundary layer

Acknowledgments

References

1. Klausmeyer, S. M., Lin, J. C., "Comparative Results From a CFD Challenge Over a 2D Three-Element High-Lift Airfoil," NASA TM 112858, May 1997.

2. Rogers, S. E., Menter, F. R., Durbin, P. A., Mansour, N. N., "A Comparison of Turbulence Models in Computing Multi-element Airfoil Flows," AIAA Paper 94-0291, January 1994.

3. Anderson, W. K., Bonhaus, D. L., McGhee, R. J., Walker, B. S., "Navier-Stokes Computations and Experimental Comparisons for Multi-element Airfoil Configurations," *J. Aircraft*, Vol. 32, No. 6, 1995, pp. 1246–1253.

4. Rumsey, C. L., Gatski, T. B., Ying, S. X., Bertelrud, A., "Prediction of High-Lift Flows using Turbulent Closure Models" *AIAA J.*, Vol. 36, No. 5, 1998, pp. 765–774.

5. Ying, S. X., Spaid, F. W., McGinley, C. B., Rumsey, C. L., "Investigation of Confluent Boundary Layers in High-Lift Flows" *Journal of Aircraft*, Vol. 36, No. 3, 1999, pp. 550–562.

6. Spaid, F. W., "High Reynolds Number, Multielement Airfoil Flowfield Measurements," *J. Aircraft*, Vol. 37, No. 3, 2000, pp. 499–507.

7. Lynch, F. T., Potter, R. C., Spaid, F. W., "Requirements for Effective High Lift CFD," International Council of the Aeronautical Sciences Proceedings, 20th Congress, Vol. 2, AIAA, Reston, VA, 1996, pp. 1479–1492.

8. Rumsey, C. L., Gatski, T. B., "Recent Turbulence Model Advances Applied to Multielement Airfoil Computations," *J. Aircraft*, Vol. 38, No. 5, 2001, pp. 904–910.

9. Jiang, F., "CFD Predictions for Control Surface Effectiveness," AIAA Paper 2000-0510, January 2000.

10. Paschal, K., Goodman, W., McGhee, R., Walker, B. Wilcox, P. A., "Evaluation of Tunnel Sidewall Boundary-Layer-Control Systems for High-Lift Airfoil Testing," AIAA Paper 91-3243, September 1991.

11. Krist, S. L., Biedron, R. T., Rumsey, C. L., "CFL3D User's Manual (Version 5.0)," NASA TM-1998-208444, June 1998.

12. Anderson, W. K., Bonhaus, D. L., "An Implicit Upwind Algorithm for Computing Turbulent Flows on Unstructured Grids," *Computers & Fluids*, Vol. 23, No. 1, 1994, pp. 1–21.

13. Anderson, W. K., Rausch, R. D., Bonhaus, D. L., "Implicit/Multigrid Algorithms for Incompressible Turbulent Flows on Unstructured Grids," *J. Comp. Phys.*, Vol. 128, 1996, pp. 391–408.

14. Spalart, P. R., Allmaras, S. R., "A One-Equation Turbulence Model for Aerodynamic Flows," *La Recherche Aerospatiale*, No. 1, 1994, pp. 5–21.

15. Bertelrud, A., "Transition on a Three-Element High Lift Configuration at High Reynolds Numbers," AIAA Paper 98-0703, January 1998.

16. Chokani, N., Kim, I., "Suppression of Pressure Oscillations in an Open Cavity by Passive Pneumatic Control," AIAA Paper 91-1729, June 1991.

17. Cao, H. V., Kusunose, K., Spalart, P. R., Ishimitsu, K. K., Rogers, S. E., McGhee, R. J., "Study of Wind Tunnel Wall Interference for Multi-element Airfoils Using a Navier-Stokes Code," AIAA Paper 94-1933, June 1994.

18. Pirzadeh, S., "Three-Dimensional Unstructured Viscous Grids by the Advancing-Layers Method," *AIAA J.*, Vol. 34, No. 1, 1996, pp. 43–49.

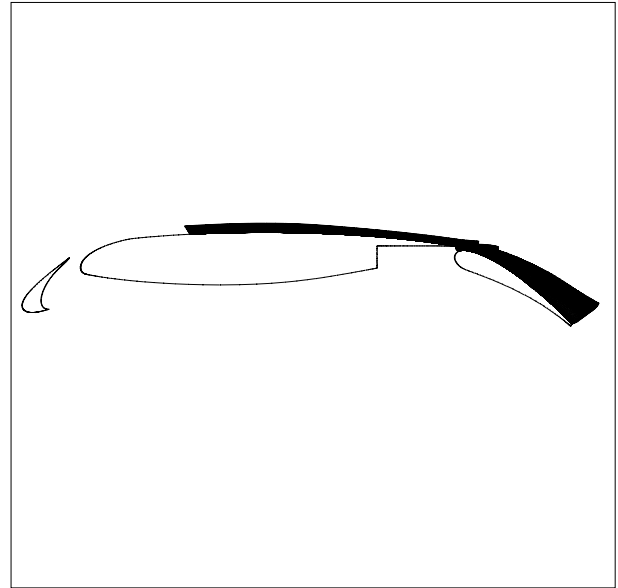Figure 2. Location of side-wall venting in the computations (Config. 2).

Figure 1. Location of side-wall venting in the experiment (dimensions in inches).
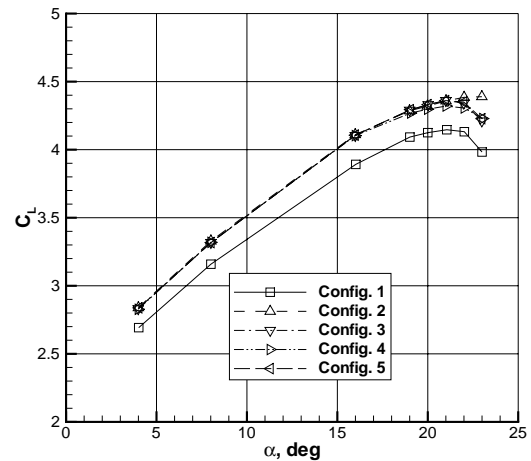
Figure 3. Lift curves in the experiment as a function of configuration.

9
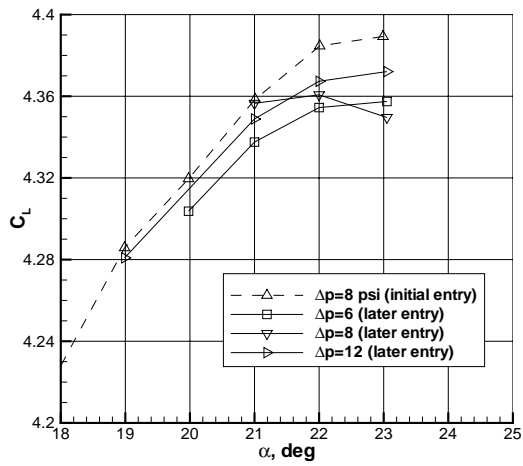
Figure 4. Effect of different venting levels near maximum lift, Config. 2.

Figure 6. Measured mass flow rates through each side wall.

Figure 5. Spanwise surface pressure coefficients on the flap upper surface, $x/c = 0.925$.

Figure 7. Photograph with superimposed sketch of oil flow pattern on wall, flap, and aft end of main for Config. 1, $\alpha = 20°$.
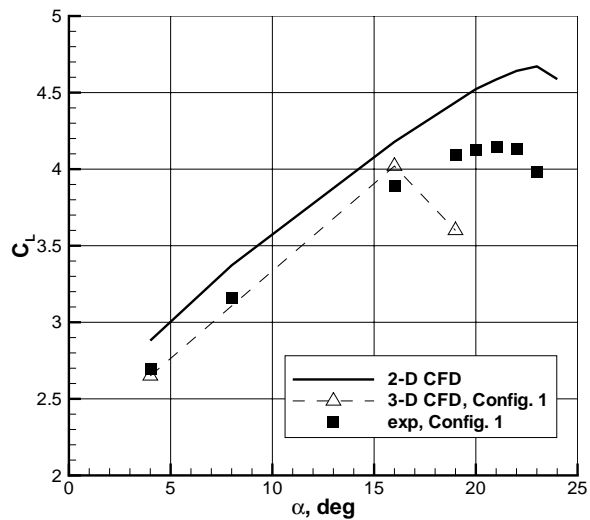
Figure 8. Lift coefficients for Config. 1.
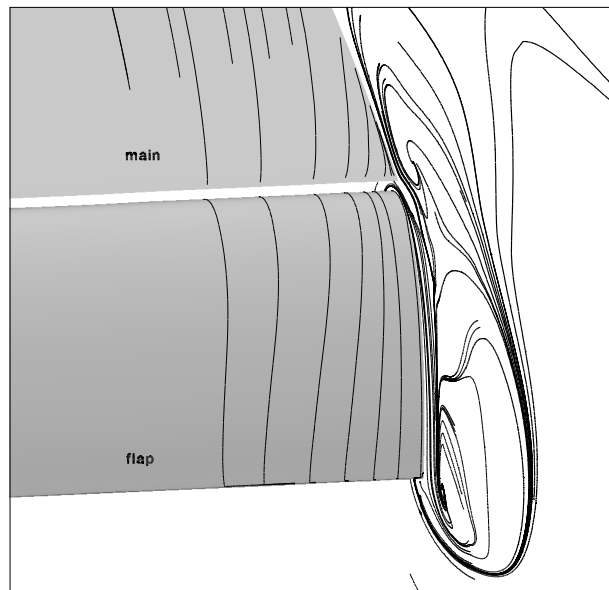
Figure 10. Computed *surface* streamlines looking upstream, Config. 1 (no venting), $\alpha = 19°$.
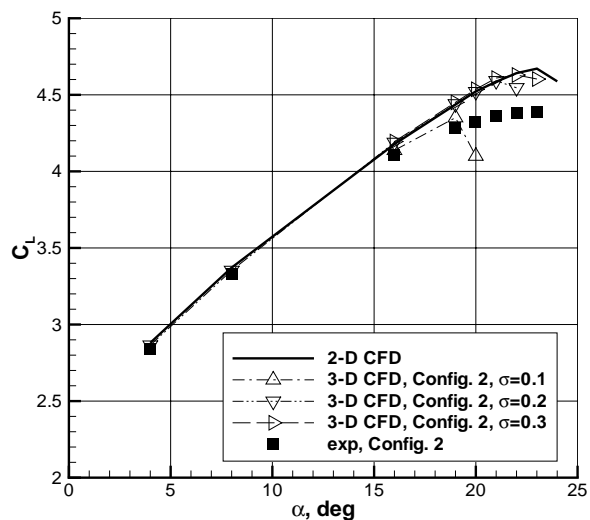
Figure 9. Lift coefficients for Config. 2.
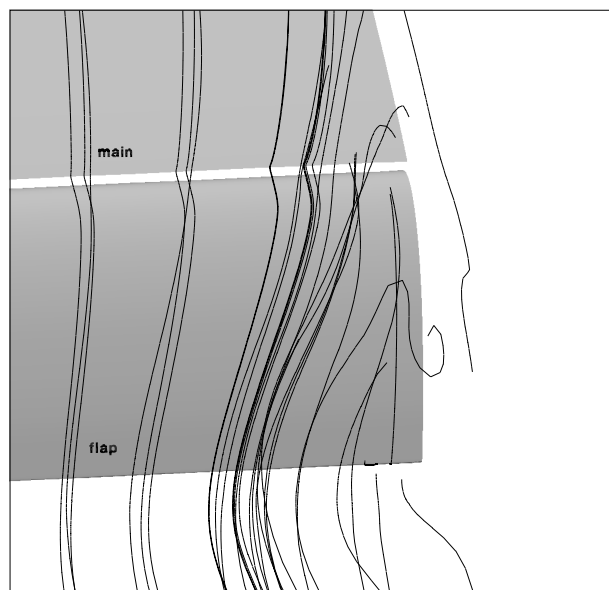
Figure 11. Computed *off-body* streamlines looking upstream, Config. 1 (no venting), $\alpha = 19°$.
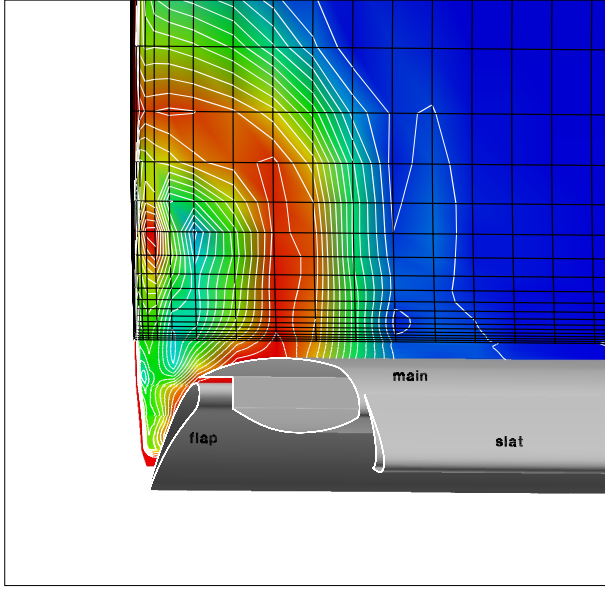
Figure 12. Vorticity contours and grid near side wall in vertical plane above trailing edge of flap, Config. 1 (no venting), $\alpha = 19°$.
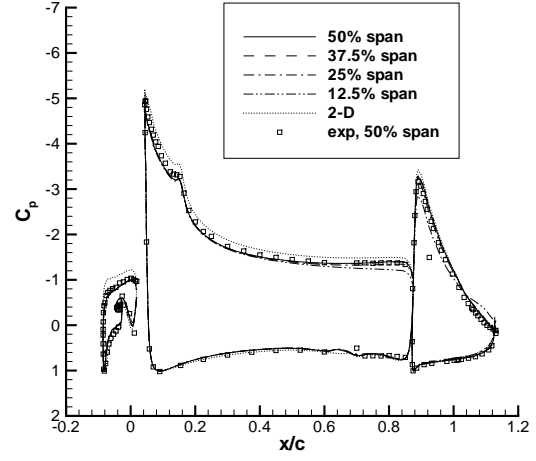
Figure 14. Chordwise surface pressure coefficients for Config. 1 (no venting), $\alpha = 4°$.
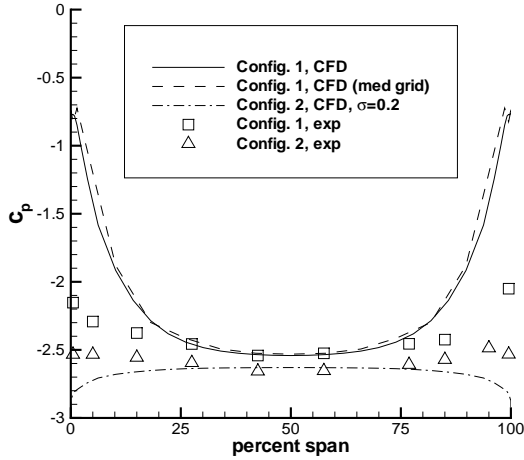
Figure 13. Spanwise surface pressure coefficients on the flap upper surface at $x/c = 0.925$, $\alpha = 4°$.
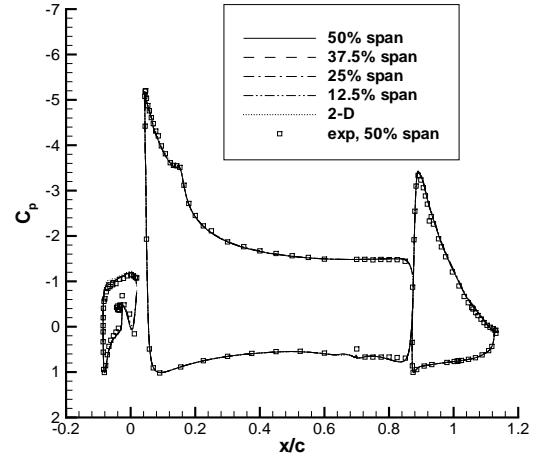
Figure 15. Chordwise surface pressure coefficients for Config. 2, $\sigma = 0.2$, $\alpha = 4°$.

American Institute of Aeronautics and Astronautics
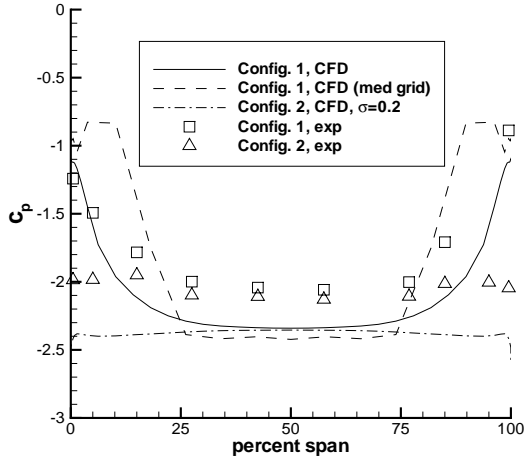
Figure 16. Spanwise surface pressure coefficients on the flap upper surface at $x/c = 0.925$, $\alpha = 16°$.
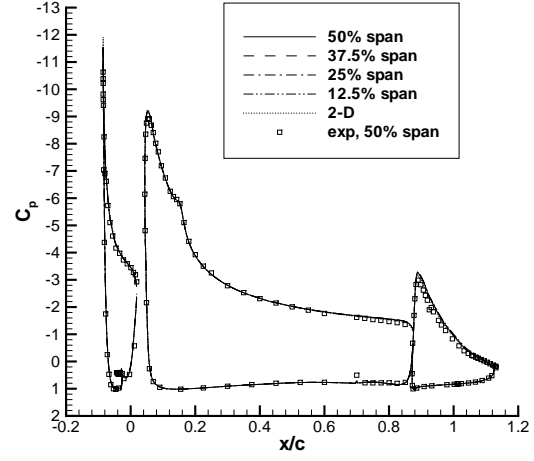
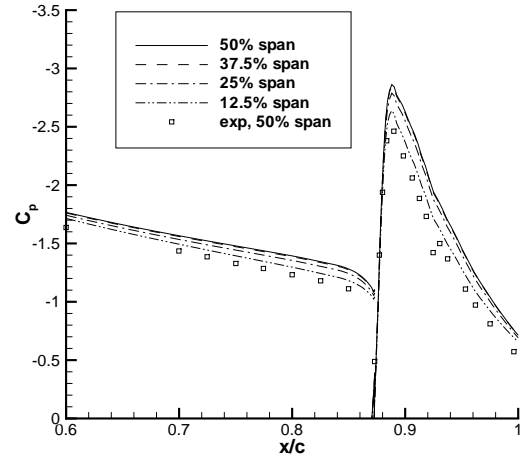Figure 18. Chordwise surface pressure coefficients for Config. 2, $\sigma = 0.2$, $\alpha = 16°$.
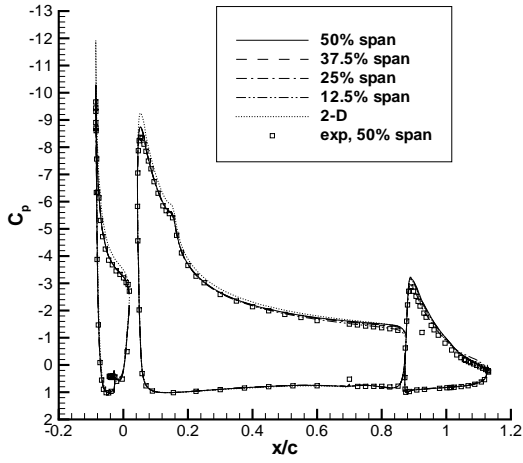
Figure 17. Chordwise surface pressure coefficients for Config. 1 (no venting), $\alpha = 16°$.
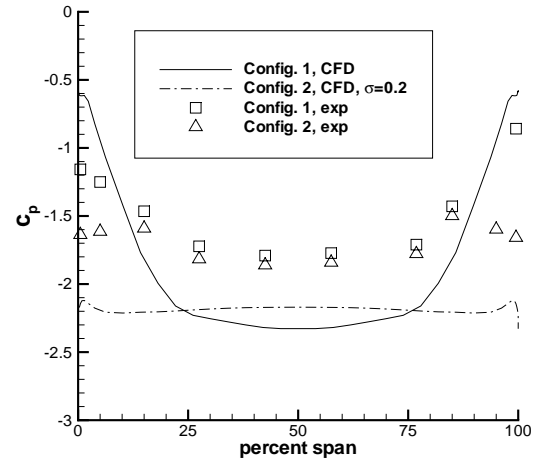
Figure 19. Spanwise surface pressure coefficients on the flap upper surface at $x/c = 0.925$, $\alpha = 19°$.
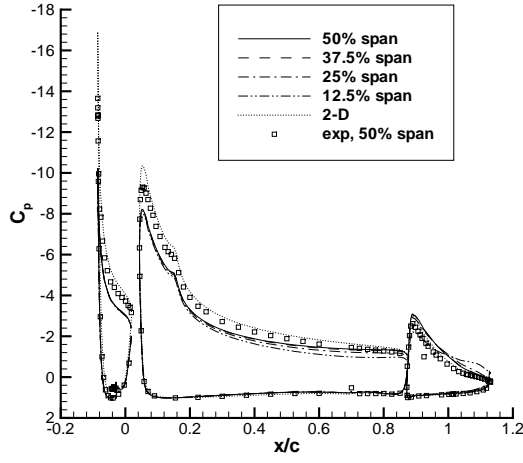
Figure 20. Chordwise surface pressure coefficients for Config. 1 (no venting), $\alpha = 19°$.
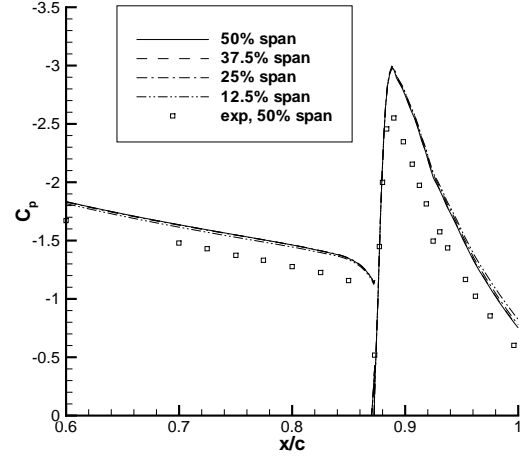
Figure 22. Close-up of chordwise surface pressure coefficients near trailing edge of main for Config. 2, $\sigma = 0.2$, $\alpha = 21°$.
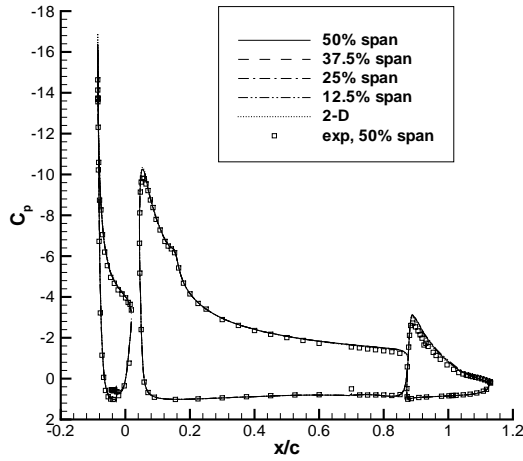
Figure 21. Chordwise surface pressure coefficients for Config. 2, $\sigma = 0.2$, $\alpha = 19°$.

Figure 23. Close-up of chordwise surface pressure coefficients near trailing edge of main for Config. 2, $\sigma = 0.2$, $\alpha = 22°$.
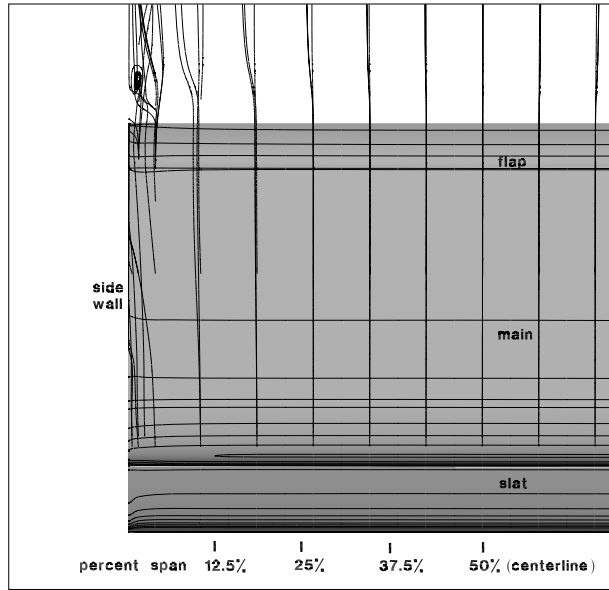
Figure 24. Computed off-body streamlines looking downstream, Config. 2, $\sigma = 0.2$, $\alpha = 19°$.
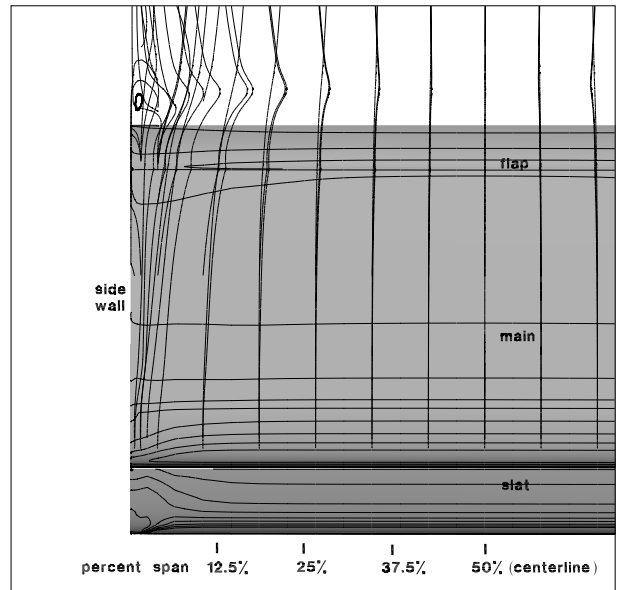
Figure 26. Computed off-body streamlines looking downstream, Config. 2, $\sigma = 0.2$, $\alpha = 22°$.
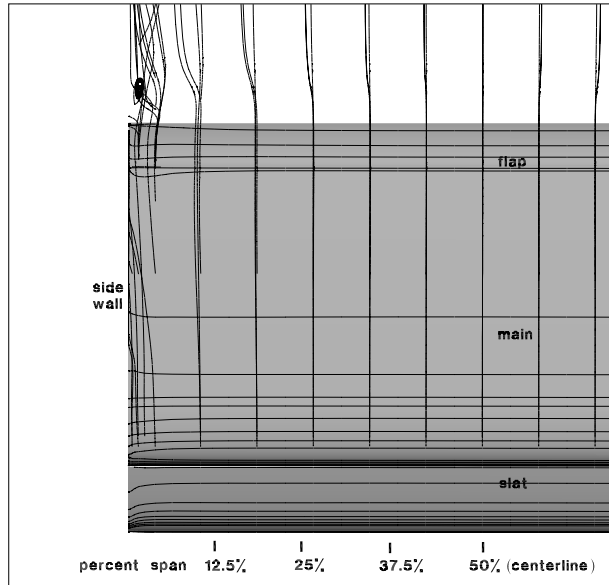
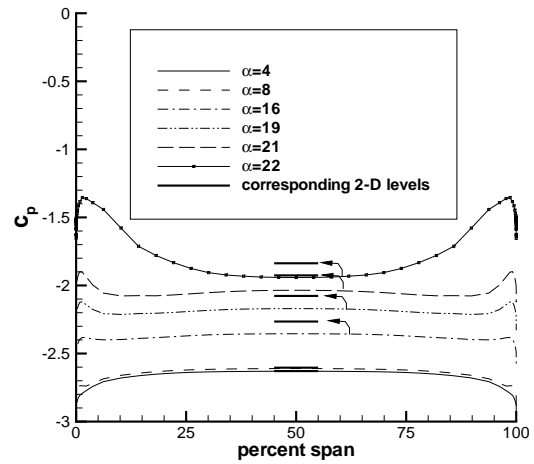Figure 25. Computed off-body streamlines looking downstream, Config. 2, $\sigma = 0.2$, $\alpha = 21°$.

Figure 27. Computed spanwise surface pressure coefficients on the flap upper surface at $x/c = 0.925$, Config. 2, $\sigma = 0.2$.
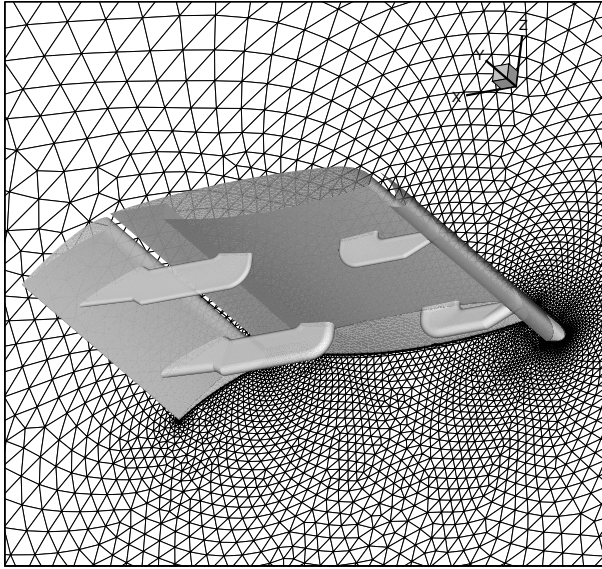
Figure 28. View of the wing surface including brackets in the unstructured grid.
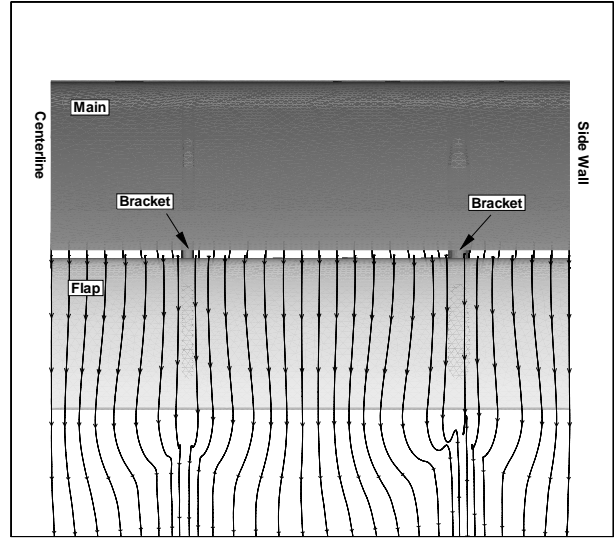

Figure 30. Computed off-body streamlines using unstructured method with brackets, looking upstream, $\alpha = 20°$.
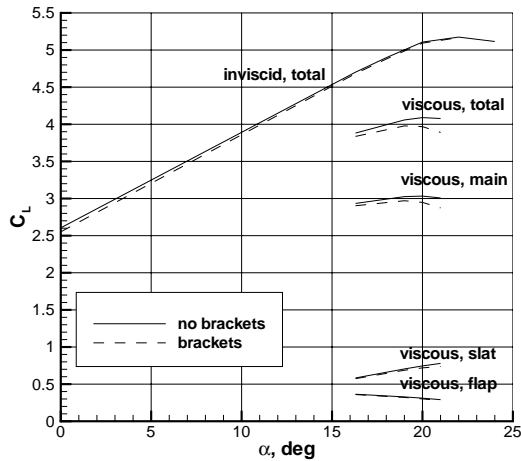

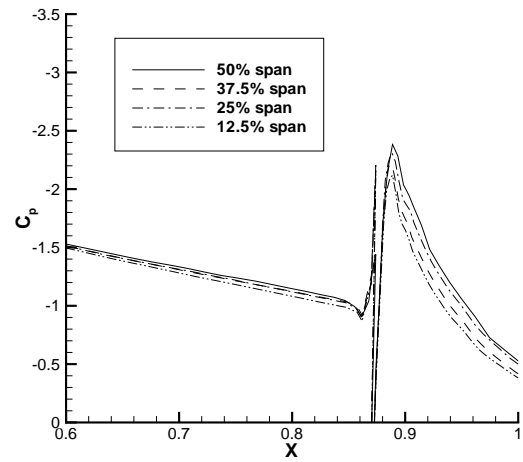Figure 29. Computed lift coefficients using unstructured method.

Figure 31. Close-up of chordwise surface pressure coefficients near trailing edge of main using unstructured method with brackets, $\alpha = 20°$.

American Institute of Aeronautics and Astronautics